Journal of Power Sources 559 (2023) 232582

Contents lists available at ScienceDirect

Journal of Power Sources

journal homepage: www.elsevier.com/locate/jpowsour

Transient hydrogen crossover in dynamically operated PEM water electrolysis cells - A model-based analysis

Tobias Franz [a], Georgios Papakonstantinou [b], Kai Sundmacher [a,b,*]

[a] Otto-von-Guericke University, Chair for Process Systems Engineering, Universitätsplatz 2, 39106, Magdeburg, Germany
[b] Max Planck Institute for Dynamics of Complex Technical Systems, Process Systems Engineering, Sandtorstr. 1, 39106, Magdeburg, Germany

HIGHLIGHTS

- Dynamic macroscopic 1-D through-plane model of a PEM electrolysis cell.
- Insights into transient hydrogen crossover phenomena.
- Simulated down steps in current density lead to transient overshoots in the H_2-in-O_2 content.
- The lower explosion limit of H_2-in-O_2 can be transiently exceeded.

GRAPHICAL ABSTRACT

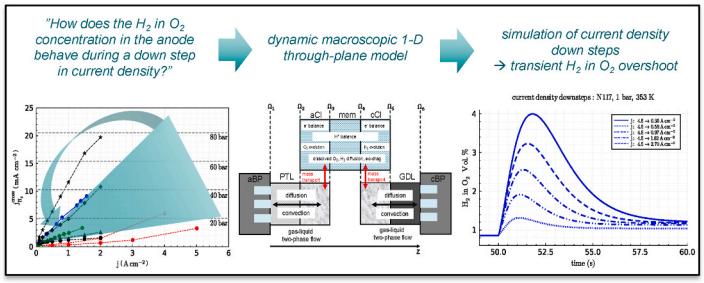

ARTICLE INFO

Keywords:
PEM water Electrolysis
Hydrogen crossover
Macroscopic modeling
Dynamic simulation

ABSTRACT

Hydrogen crossover in polymer electrolyte membrane electrolysis cells is important concerning faradaic efficiency, flammability hazards, and degradation phenomena. In recent years, steady-state H_2-in-O_2 measurements have demonstrated that the hydrogen crossover increases with current density, due to mass transport limitations in the cathode catalyst layer. However, hydrogen crossover during dynamic operation has not been investigated yet. Therefore, this study investigates the hydrogen crossover with a dynamic macroscopic 1-D through-plane model of a polymer electrolyte membrane electrolysis cell. The model focuses on the detailed description of the dynamics of the reactions and mass transport of hydrogen in the membrane electrode assembly. Simulated down steps in current density, lead to transient overshoots in the H_2-in-O_2 content at the anode side. The membrane acts as short-term mass storage for the dissolved hydrogen, and mass transport lags the instant response of the current density. Under specific conditions with high cathode mass transport limitations, the lower explosion limit of H_2-in-O_2 can be transiently exceeded. This work provides for the first-time insights into transient hydrogen crossover phenomena and is a further step into dynamic model-based analysis of polymer electrolyte water electrolysis cells.

1. Introduction

Hydrogen crossover in polymer electrolyte membrane (PEM) electrolysis cells is an important phenomenon that influences faradaic efficiency, flammability hazards, and degradation phenomena [1]. Previous research has documented that the hydrogen crossover

* Corresponding author. Otto-von-Guericke University, Chair for Process Systems Engineering, Universitätsplatz 2, 39106, Magdeburg, Germany.
E-mail address: sundmacher@mpi-magdeburg.mpg.de (K. Sundmacher).

https://doi.org/10.1016/j.jpowsour.2022.232582
Received 4 October 2022; Received in revised form 8 December 2022; Accepted 22 December 2022
Available online 11 January 2023

increases with temperature, cathode hydrogen partial pressure, and current density [2–9]. In recent years, the increase of the hydrogen crossover flux with current density was studied and discussed by several groups in more detail [3,9–14]. In these studies, the increase of hydrogen crossover varies strongly and can be equivalent to partial hydrogen pressures in the cathode of several bar per A cm^{-2}. In general, this phenomenon can be explained by a local pressure build-up [3] or by supersaturation of dissolved hydrogen in the cathode catalyst layer [10], due to limited transport of evolving hydrogen from the catalyst into the pore space [3,10,12]. Based on the model investigations by Trinke et al., the supersaturation concept seems more plausible [10,15]. Additionally, it was discovered that the mass transport limitations in the cathode catalyst layers are enhanced by high cathode catalyst layer ionomer contents and high compression forces [12–14,16].

Although several works studied the increase of hydrogen crossover with current density under steady-state conditions, no attention has been paid to hydrogen crossover during dynamic operation. Flexible dynamic operation of PEM electrolyzers can offer attractive revenues, which can reduce the production costs of hydrogen. For example, frequency control services can be offered to electrical grid operators through short periods of increased or decreased power consumption in the electrolysis operation [17,18]. Concerning hydrogen permeation, the dynamic operation from high to low current densities needs to be considered in more detail. At high current densities, the supersaturated concentration of dissolved hydrogen in the membrane electrode assembly (MEA) leads to increased hydrogen crossover. At the same time, the increased hydrogen crossover flux is diluted in the anode by the high formation rates of oxygen. If the current density is suddenly reduced, the oxygen production rate will drop instantly. However, the hydrogen permeation to the anode side will still be enhanced, as the membrane may act as a mass storage capacity for the dissolved supersaturated hydrogen. Based on these considerations, a transient overshoot of the hydrogen in oxygen concentration in the anode is predicted for a down step from high to low current density. This leads to the following question: *"How does the hydrogen in oxygen content behave during a down step in current density?"* The magnitude of this overshoot may even exceed the lower explosion limit (LEL) on the anode side amid dynamic operating conditions. Furthermore, excessively high H_2 contents in the anode may influence catalyst degradation. It has been demonstrated that Ir oxide interacts with the permeated H_2 [11] and it reduces under open circuit conditions at rich H_2 conditions [1]. Meanwhile, dynamic operation has been associated with an accelerating increase of the cell resistance [11,19–21].

Capturing the dynamics of the hydrogen crossover is not possible with the experimental set-ups used in steady-state hydrogen crossover measurements, in which the hydrogen in oxygen concentration is measured downstream the gas separator and condenser [10,11,13]. The dynamic measurement of the hydrogen in oxygen concentration directly at the anode outlet appears to be difficult, due to the complex two-phase gas-liquid flow. Therefore, the dynamic hydrogen crossover is studied in this work with a dynamic macroscopic 1-D through-plane model of a PEM electrolysis cell.

Recent publications [22–25] give a good review on general macroscopic modeling of electrochemical cells, and specifically of PEM electrolysis cells. Several discretized macroscopic models studied the two-phase flow in the porous transport layers [26–29]. The water transport inside the membrane in vapor-fed PEM electrolysis cell was investigated by Fornaciari et al. [30] with a macroscopic 2-D model. Garcia-Salaberri [31] developed a comprehensive 1-D through plane model, but without considering the gas crossover in the membrane. The first detailed 1-D steady-state model describing the increased gas crossover and supersaturation effect was developed by Trinke [15]. However, there is a lack of dynamic water electrolysis models in literature [23]. In addition, Etzold et al. [23] highlighted the importance of dynamic model analysis for better model validation and insights into reaction and transport processes with different time constants. Moreover, dynamic model formulations allow deriving model-based electrochemical impedance or even non-linear frequency response analysis spectra for further analysis of nonlinear electrochemical systems [32].

This work contributes to the understanding of dynamic gas crossover phenomena, as well as to the development of dynamic macroscopic models and the simulation of electrochemical cells in general. To study the dynamic H_2-in-O_2 content at the anode, the 1-D dynamic macroscopic model is formulated and parametrized with experimental steady-state hydrogen crossover measurements from literature. Furthermore, the influence of the electroosmotic drag on the hydrogen crossover is discussed. During current density down steps, the H2-in-O2 content at the anode side and the through-plane profile in the MEA are analyzed. The influence of temperature, pressure, membrane thickness and the anode water flow rate are also investigated.

2. Methods - model description

The model domain is schematically shown in Fig. 1. The macroscopic model includes the channels, the porous transport layers, the catalyst layers and the membrane. The whole model is isothermal, consequently, only mass and charge balances are solved in the different layers. The channels are each modeled as a control volume based on an isobar and isotherm continuous stirred-tank reactor (CSTR) approach with the assumption of equal gas and liquid water outlet velocity.

The mass balances in the channels and catalyst layers (aCl, cCl) are connected by simple Darcy's-Law two-phase-flow equations in the porous transport layers (PTL, GDL). The catalyst layers are modeled by a macroscopic porous electrode approach and consist of a solid electrically conductive phase, a proton conductive liquid water saturated ionomer phase, and a pore space filled with gas and liquid. Each of these phases has a specific volume fraction in the catalyst layer, which can be calculated from the catalyst loading, the ionomer content, and the catalyst layer thickness. To include the supersaturation phenomena, hydrogen and oxygen are modeled to be produced in the dissolved gas form in the water saturated ionomer phase of the cathode- and anode catalyst layer, respectively.

In the catalyst layers, the electron and proton charge balances plus the mass balances of oxygen and hydrogen in the dissolved form are derived. The mass transport of the liquid water and the gas phases in the pore space is described by two-phase flow equations, similarly to the porous transport layers. The connection between the dissolved gas concentration in the ionomer and the gas phase partial pressures in the pore space of the catalyst layer is modeled by a mass transfer coefficient.

Based on experimental results in literature, it is well known that the high-frequency resistance (HFR) of a medium-loaded MEA (1–2 mg_{Ir} cm^{-2}) is independent of current density or even decreases due to increasing waste heat production, leading to an increased membrane temperature and a higher ionic conductivity [33–35]. An increase in the HFR with current density was measured only for high iridium loading (≈4 mg_{Ir} cm^{-2}) and the resulting thick catalyst layer. This effect was explained by a slight drying-out of the membrane, due to the increased mass transport resistance of liquid water in a thick electrode [34]. Consequently, the membrane and the ionomer phase in the catalyst layers are assumed fully saturated and in equilibrium with liquid water, resulting in a constant bulk ionomer conductivity. Therefore, the water transport in the ionomer phase of the catalyst layers and the membrane is not modeled. To account for the electroosmotic water drag, sinks and sources are introduced in the liquid water balance in the anode- and cathode catalyst layer pore space.

2.1. Potential fields

The equations used to simulate the potential fields are based on the macroscopic porous electrode model described by Vidaković-Koch et al. [36]. The proton balances are formulated in the anode and cathode

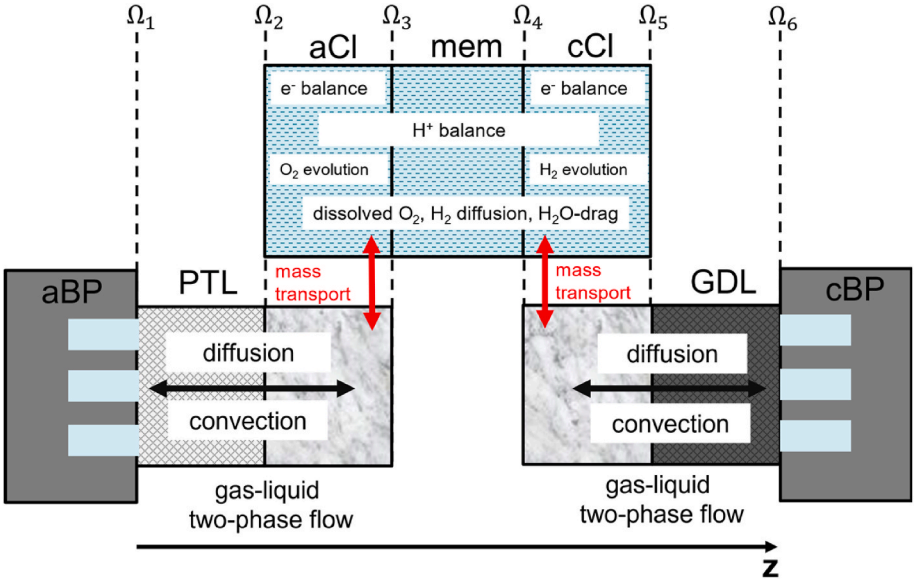

Fig. 1. Schematic representation of the 1-D model domains and the interfaces Ω_i between the domains. The z-axis is the direction of the spatial discretization.

catalyst layer, as well as in the membrane. The membrane is assumed as an electric insulator. Therefore, the electron charge balances are only valid in the catalyst layers. The porous transport layer (PTL) and gas diffusion layer (GDL) are each considered by an additional electrical resistance.

2.1.1. Balance equations

The electric potential φ_E in the catalyst layers follows from the charge balance for the electron conductor

$$0 = -\frac{\partial}{\partial z}\left(-\sigma_{cat}^{eff}\frac{\partial \varphi_E}{\partial z}\right) + aj \tag{1}$$

where σ_{cat}^{eff} is the effective electrical conductivity of the catalyst, j the local charge production density and a the surface of the catalyst per unit volume of the electrode. The proton potential φ_P in the catalyst layers and membrane can be calculated from the charge balance in the ionomer

$$0 = -\frac{\partial}{\partial z}\left(-\sigma_P^{eff}\frac{\partial \varphi_P}{\partial z}\right) - aj. \tag{2}$$

In equations (1) and (2), the effective electrical conductivity σ_{cat}^{eff} and the effective ionomer conductivity σ_P^{eff} are given by the Brueggemann approach as

$$\sigma_E^{eff} = \frac{\varepsilon_{cat}}{\tau_{cat}}\sigma_{cat} \quad \sigma_P^{eff} = \frac{\varepsilon_P}{\tau_P}\sigma_P \tag{3}$$

with $\varepsilon_{cat}, \varepsilon_P$ and τ_{cat}, τ_P the volume fraction and the tortuosity of the catalyst and ionomer phases, respectively. The tortuosity can be estimated by the Brueggemann's correlation $\tau = \sqrt{1/\varepsilon}$. The calculation of the volume fractions of catalyst, ionomer, and pore space, as well as the values of the bulk conductivitiescan be found in the supporting information in section S1 and S3, respectively. The surface of the catalyst a can be formulated as

$$a = a_0\frac{L_{cat}}{d_{cat}} \tag{4}$$

where a_0 is the catalyst surface area per unit mass of the catalyst, while L_{cat} is the catalyst loading and d_{cat} is the thickness of the catalyst layer.

The spatially distributed overpotential in the catalyst layer is defined as

$$\eta = \varphi_E - \varphi_P - \Delta\varphi^{rev} \tag{5}$$

with $\Delta\varphi^{rev}$ the reversible potential of the electrode.

The reversible potentials of the anode $\Delta\varphi_a^{rev}$ and cathode $\Delta\varphi_c^{rev}$ are described by the Nernst equation (6) and (7).

$$\Delta\varphi_a^{rev} = \Delta\varphi_a^0(T) + \frac{RT}{2F}\ln\left(\sqrt{\frac{c_{O_2,diss}}{c_{O_2,diss}^0}}\right) \tag{6}$$

$$\Delta\varphi_c^{rev} = \Delta\varphi_c^0 - \frac{RT}{2F}\ln\left(\frac{c_{H_2,diss}}{c_{H_2,diss}^0}\right) \tag{7}$$

where $c_{O_2,diss}$ and $c_{H_2,diss}$ are the dissolved gas concentrations of oxygen and hydrogen in the electrode ionomer liquid phase. The equivalent dissolved gas concentrations at standard conditions of 1 bar are described by $c_{O_2,diss}^0$ and $c_{H_2,diss}^0$. The standard reversible potential of the anode $\Delta\varphi_a^0(T)$ is a function of temperature [15]

$$\Delta\varphi_a^0 = 1.478 - 8.347 \bullet 10^{-4}\, T \tag{8}$$

The standard reversible potential of the cathode $\Delta\varphi_c^0$ is set per definition to 0 V.

2.1.2. Kinetics

The local charge production density j in the cathode catalyst layer is given by the Butler-Volmer equation

$$j = j_0\, exp\left(\frac{2.303}{b_a}\eta\right) - exp\left(-\frac{2.303}{b_c}\eta\right) \tag{9}$$

where b_a and b_c represent the anodic (HOR) and cathodic (HER) Tafel slopes, and j_0 the exchange current density per surface of the catalyst. The Tafel slopes and exchange current density of the cathode catalyst are taken from rotating disk electrode experiments from Durst et al. [37]. In the anode catalyst layer the Tafel equation is used and the exchange current density and Tafel slope of the anode catalyst are fitted to experimental data from Martin et al. [14] in the low current density range as shown in the supporting information, in Fig. S3b. An overview of the electrochemical kinetic parameters used in the anode and cathode catalyst layer can be found in the SI, Table S1.

2.1.3. Boundary conditions

In galvanostatic mode, the electric current density at the anode channel/PTL interface Ω_1 and GDL/cathode channel interface Ω_6 is set to the applied current density.

$$-\sigma_E^{eff}\frac{\partial\varphi_E}{\partial z}|\Omega_i = j_{applied} \quad i=1,6 \tag{10}$$

The electric potential at the GDL/cathode channel interface Ω_6 is set to zero and the electric potential at the anode channel/PTL interface Ω_1 is the overall cell voltage U_{cell}.

$$\varphi_E(\Omega_6)=0 \tag{11}$$

$$\varphi_E(\Omega_1)=U_{cell} \tag{12}$$

The membrane is assumed to not conduct electrons, consequently a no-flux boundary condition is imposed for the electric potential at the acl/mem interface Ω_3 and for the ccl/mem interface Ω_4.

$$-\sigma_E^{eff}\frac{\partial\varphi_E}{\partial z}\bigg|_{\Omega_i}=0 \quad i=3,4 \tag{13}$$

Similarly, a no-flux boundary condition is implemented for the proton potential at the acl/PTL interface Ω_2 and ccl/GDL interface Ω_5.

$$-\sigma_P^{eff}\frac{\partial\varphi_P}{\partial z}\bigg|_{\Omega_i}=0 \quad i=2,5 \tag{14}$$

2.2. Dissolved gas concentration fields

The transport of dissolved gases in the water-filled ionomer is considered only in the catalyst layers and the membrane. The dynamic mass balances for the dissolved hydrogen and oxygen are formulated in the concentration form as follows

$$\frac{\partial c_{\alpha,diss}}{\partial t}=\frac{1}{\varepsilon_P\,\varepsilon_{H_2O,ion}}\left(-\frac{\partial}{\partial z}\left(-D_{\alpha,diss}^{eff}\frac{\partial c_{\alpha,diss}}{\partial z}+\frac{n_{drag}c_{\alpha,diss}}{Fc_{H_2O}}j\right)+\Gamma_{\alpha,prod}-\Gamma_{\alpha,mass}\right) \quad \alpha=H_2,O_2 \tag{15}$$

where $c_{\alpha,diss}$ are the dissolved gas concentrations, c_{H_2O} the molar concentration of liquid water, ε_P is the ionomer volume fraction, $\varepsilon_{H_2O,ion}$ the volume fraction of water within the ionomer and $D_{\alpha,diss}^{eff}$ the effective diffusion coefficient of the dissolved gases, which is given by

$$D_{\alpha,diss}^{eff}=\frac{\varepsilon_P\varepsilon_{H_2O}}{\tau_P}D_{\alpha,diss} \quad \alpha=H_2,O_2 \tag{16}$$

with τ_P the tortuosity of the ionomer. The calculation of the diffusion coefficient of dissolved hydrogen and oxygen in pure water $D_{\alpha,diss}$, as a function of temperature can be found in supporting information, section S1.

The production term $\Gamma_{\alpha,prod}$ in equation (*15*) is only active in the anode catalyst layer for oxygen and in the cathode catalyst layer for hydrogen. The production rates of hydrogen and oxygen in the catalyst layers in the dissolved form can be calculated as follows

$$in\ ccl: \quad \Gamma_{H_2,prod}=\frac{|aj|}{2F} \quad \Gamma_{O_2,prod}=0 \tag{17}$$

$$in\ acl: \quad \Gamma_{H_2,prod}=0 \quad \Gamma_{O_2,prod}=\frac{aj}{4F} \tag{18}$$

The term $\Gamma_{\alpha,mass}$ in equation (*15*) describes the mass transport of hydrogen and oxygen from the dissolved phase through the ionomer to the gas phase in the catalyst layer pore space and is defined as

$$\Gamma_{\alpha,mass}=k_{\alpha,mass}\left(c_{\alpha,diss}-c_{\alpha,sat}\right) \quad \alpha=H_2,O_2 \tag{19}$$

where $k_{\alpha,mass}$ is the mass transport coefficient and $c_{\alpha,sat}$ the concentration of the saturated dissolved gas. The mass transport coefficient $k_{\alpha,mass}$ determines the strength of the occurring supersaturation and is a yet unknown complex function of parameters, such as current density, temperature, pressure, liquid saturation, and local position and is influenced by the structural properties of the catalyst layer, such as the catalyst and ionomer loadings [12,16]. Furthermore, external influences, such as the compression forces on the MEA, can change the structural properties in the catalyst layer and thus alter the mass transport coefficient [14]. In a model-based analysis, Trinke linked the mass transport coefficient with the ionomer content in the catalyst layer and showed good agreement with experimental hydrogen crossover data [15]. However, there is not yet a unified approach to describe quantitatively the overall span in H2 permeation data, as well as the strong nonlinear hydrogen crossover increase observed in some studies [9, 12–14]. As a simplification, the cathode mass transport coefficient is fitted to steady-state experimental hydrogen crossover data from literature, to reproduce the linear behavior.

The saturated dissolved gas concentration is calculated by Henry's law

$$c_{\alpha,sat}=p_\alpha S_{\alpha-H_2O} \quad \alpha=H_2,O_2 \tag{20}$$

with $S_{\alpha-H_2O}$ the solubility of hydrogen or oxygen in pure water and p_α the partial pressure of the gas in the pore space of the catalyst layer. The calculation of the temperature dependent solubilities of hydrogen and oxygen in pure water can be found in the supporting information, section S1. In the membrane, no reaction or mass transport from dissolved to the gas phase occurs, and the dynamic mass balance is governed by diffusion and the convective effect of the electroosmotic drag. The recombination of oxygen and hydrogen back to water, by e.g. Platinized-PTLs [2,5] or recombination catalysts [38,39] and interlayers [35,40, 41], can influence the local concentration and their profiles, but in the absence of detailed information on recombination kinetics and oxygen crossover [42] it is not considered in this model formulation.

2.2.1. Boundary conditions

The dissolved gas transport in the water-filled ionomer is continuous at the interfaces between the catalyst layers and the membrane (Ω_3,Ω_4). At the PTL/acl and ccl/GDL interfaces (Ω_2,Ω_5) no-flux boundary conditions are applied for the hydrogen and oxygen mass balance as follows

$$-D_{H_2,diss}^{eff}\frac{\partial c_{H_2,diss}}{\partial z}+\frac{n_{drag}c_{\alpha,diss}}{Fc_{H_2O}}j\bigg|_{\Omega_i}=0 \quad i=2,5 \tag{21}$$

$$-D_{O_2,diss}^{eff}\frac{\partial c_{O_2,diss}}{\partial z}+\frac{n_{drag}c_{\alpha,diss}}{Fc_{H_2O}}j\bigg|_{\Omega_i}=0 \quad i=2,5 \tag{22}$$

The gases are produced and can be transported in the dissolved form in the water filled ionomer of the catalyst layers and the membrane. The transport of the dissolved gases beyond these boundaries is only possible by the mass transfer from the dissolved gas phase in the catalyst layers to the gas filled pore space via Eq. (*19*).

2.3. Two-phase gas and liquid flow

The mass transport in the pore space of the catalyst layers, as well as in the PTL and GDL is described by a two-phase flow of a compressible gas phase and an incompressible liquid water phase. The gas phase consists of hydrogen, oxygen, and water vapor

$$p_g=p_{H_2}+p_{O_2}+p_{H_2O,g} \tag{23}$$

The gas phase pressure p_g and the liquid phase pressure p_l are connected by the capillary pressure p_c, which is a function of the liquid saturation s_l in the pore space as described in the supporting information

S2

$$p_c(s_l) = p_g - p_l \tag{24}$$

The transport of the gas and liquid phase through porous media is modeled by Darcy's law, which is an oversimplification of the complex capillary-dominated transport [43]. To study the two-phase-flow behavior, more realistic and complex models should be used instead [44]. In this work, however, the focus lies on the coupled dynamic reaction-transport processes of the dissolved gases in the MEA, therefore the assumption of Darcy's law is considered. The resulting equations are three dynamic mass balances in the partial pressure form and one dynamic mass balance in the liquid saturation form. The dynamic mass balances for the partial pressures of hydrogen, oxygen, and water vapor in the gas phase are

$$\frac{\partial p_\alpha}{\partial t} = \frac{1}{(1-s_l)}\left(\frac{1}{\varepsilon_{pore}}\left(-\frac{\partial p_\alpha u_g}{\partial z} - \frac{\partial J_{diff,\alpha}}{\partial z} + \Gamma_{\alpha,mass} RT\right) + p_\alpha \frac{\partial s_l}{\partial t}\right) \quad \alpha = H_2, O_2, H_2O \tag{25}$$

$$J_{diff,\alpha} = -D^{eff}_{\alpha-\beta}\frac{\partial p_\alpha}{\partial z} \quad \alpha = H_2, O_2, H_2O \tag{26}$$

$$u_g = -\frac{k_{r,g}\,K}{\mu_g}\left(\frac{\partial p_g}{\partial z}\right) \tag{27}$$

where p_α is the partial pressure in the gas phase, ε_{pore} the volume fraction of the pore space and u_g the gas phase velocity. The relative gas permeability $k_{r,g}$, the hydraulic permeability K of the porous media, the dynamic viscosity μ_g of the gas phase, and the effective gas phase binary diffusion coefficients $D^{eff}_{\alpha-\beta}$ are defined and calculated in the supporting information S2. The mass transport term $\Gamma_{H_2O,mass}$ is a connection between the water vapor in the gas phase and the liquid water phase and takes evaporation or condensation of water into account as follows

$$\Gamma_{H_2O,mass} = \frac{k_{eva}}{RT}\left(p^{sat}_{H_2O,g} - p_{H_2O,g}\right) \tag{28}$$

with k_{eva} being the evaporation/condensation coefficient and $p^{sat}_{H_2O,g}$ the saturated water vapor pressure, which is calculated by the Magnus formula [45] in the supporting information S2. The gas phase is assumed to be always fully saturated with water vapor, hence the evaporation/condensation coefficient is set to an infinitely large number. The dynamic mass balance for the liquid saturation is formulated by

$$\frac{\partial s_l}{\partial t} = -\frac{1}{\varepsilon_{pore}}\left(\frac{\partial}{\partial z}\left(-\frac{k_{r,l}\,K}{\mu_l}\left(\frac{\partial p_l}{\partial z}\right)\right) + \left(\Gamma_{H_2O,react} + \Gamma_{H_2O,drag} - \Gamma_{H_2O,mass}\right)\overline{V}_{H_2O}\right) \tag{29}$$

where $k_{r,l}$ is the relative liquid permeability, μ_l the dynamic viscosity of liquid water and $\overline{V}_{H_2O}$ the molar volume of liquid water, which are defined in the supporting information, section S2. In equation (*29*), the term $\Gamma_{H_2O,react}$ describes the consumption of liquid water due to the electrochemical reaction, which is only active in the anode catalyst layer. The electroosmotic water drag ($n_{drag} = 2.5$ [46]) is affecting the liquid saturation balance in both catalyst layers and is described by the term $\Gamma_{H_2O,drag}$. Both terms are defined as follows

$$in\ acl: \quad \Gamma_{H_2O,react} = -\frac{aj}{2F} \quad \Gamma_{H_2O,drag} = -\frac{ajn_{drag}}{F} \tag{30}$$

$$in\ ccl: \quad \Gamma_{H_2O,react} = 0 \quad \Gamma_{H_2O,drag} = \frac{ajn_{drag}}{F} \tag{31}$$

2.3.1. Boundary conditions

The dynamic two-phase flow mass balances are only valid in the porous transport layers (PTL, GDL) and the catalyst layers (acl, ccl), thus no two-phase fluxes are leaving or entering through the catalyst layers/membrane interfaces (Ω_3, Ω_4). At the anode channel/PTL and cathode channel/GDL interfaces (Ω_1, Ω_6) the following boundary conditions apply

$$p_\alpha(\Omega_1) = p_\alpha^{aCh} \quad s_l(\Omega_6) = {s_l}^{aCh} \tag{32}$$

$$p_\alpha(\Omega_6) = p_\alpha^{cCh} \quad s_l(\Omega_6) = {s_l}^{cCh} \tag{33}$$

with p_α^{aCh} and p_α^{cCh} being the partial pressures of the gases in the anode and cathode channel and ${s_l}^{aCh}, {s_l}^{cCh}$ the liquid saturations in the channels.

2.4. Mass balance in the channels

The anode and cathode channels are modeled by an CSTR approach, similar to that described by Kim et al. [47]. The difference in this work is that the model is not discretized along the channel coordinate and the channels are each approximated as one isothermal isobar control volume. In the channels exists a liquid water phase and a gas phase, which consists of hydrogen, oxygen, and water vapor. The dynamic mass balances of the gas phase in the concentration form can be formulated as follows

$$\frac{dc_\alpha}{dt} = \frac{\left(u^{in}_{g,ch}c^{in}_\alpha - u^{out}_{g,ch}c^{out}_\alpha\right)}{l_{ch}} + \frac{1}{h_{ch}}\left(+\dot{n}_{\alpha,conv} + \dot{n}_{\alpha,diff}\right) \quad \alpha = H_2, O_2, H_2O \tag{34}$$

where c_α is the gas concentration with respect to the whole channel volume, $u_{g,ch}$ the gas phase velocity in the channel, h_{ch} the channel height. The convective and diffusive terms that enter the channels from the porous transport layers at the interfaces Ω_1 and Ω_6 are represented by the terms $\dot{n}_{\alpha,conv}$ and $\dot{n}_{\alpha,diff}$, respectively. The dynamic mass balance of liquid water can be written as follows

$$\frac{dc_{H_2O,l}}{dt} = \frac{\left(u^{in}_{l,ch}c^{in}_{H_2O,l} - u^{out}_{l,ch}c^{out}_{H_2O,l}\right)}{l_{ch}} + \frac{1}{h_{ch}}\left(\dot{n}_{H_2O,conv}\right) \tag{35}$$

with $c_{H_2O,l}$ being the liquid water concentration in the whole channel volume, $u_{l,ch}$ the liquid water velocity in the channel and $\dot{n}_{H_2O,conv}$ the convective liquid water flux entering or leaving at the channel/porous transport layers interfaces (Ω_1, Ω_6). One of the main simplifications is the assumption of equal gas- and liquid-phase velocities $u_{g,ch} = u_{l,ch}$ in the channels, which means that only one additional equation is needed to calculate the channel velocity. This additional equation can be derived from the fact that the total channel volume V_{ch} is the sum of the gas and liquid volumes as follows

$$V_{ch} = V_{H_2} + V_{O_2} + V_{H_2O,g} + V_{H_2O,l} \tag{36}$$

The gas volumes V_a and the liquid volume $V_{H_2O,l}$ can be expressed as follows

$$V_a = \frac{c_a V_{ch} RT}{p^{ch}} \quad V_{H_2O,l} = \frac{c_{H_2O,l} M_{H_2O} V_{ch}}{\rho_{H_2O}} \tag{37}$$

Furthermore, the total channel volume is constant and does not depend on time

$$\frac{dV_{ch}}{dt} = 0 = \frac{dV_{H_2}}{dt} + \frac{dV_{O_2}}{dt} + \frac{dV_{H_2O,g}}{dt} + \frac{dV_{H_2O,l}}{dt} \tag{38}$$

Consequently equation (*38*) transforms with the expressions in equation (*37*) to

$$0 = \frac{V_{ch}RT}{p^{ch}}\left(\frac{\partial c_{O_2}}{\partial t} + \frac{\partial c_{H_2}}{\partial t} + \frac{\partial c_{H_2O,g}}{\partial t}\right) + \frac{M_{H_2O}V_{ch}}{\rho_{H_2O}}\frac{\partial c_{H_2O,l}}{\partial t} \tag{39}$$

2.4.1. Inlet water flow rate

The cathode is assumed without a water inlet flow. The anode inlet water flow rate $\dot{F}_{H_2O}^{anode}$ is calculated as follows

$$\dot{F}_{H_2O}^{a} = \frac{(U_{cell} - 1.48\ V)j}{c_{p,H_2O}\Delta T\ \rho_{H_2O}} \tag{40}$$

where U_{cell} is the operational cell voltage in Volt, 1.48 V the thermoneutral cell voltage, j the operational current density in A m^{-2}, c_{p,H_2O} the specific heat capacity of liquid water (4180 kJ/(kg K)) and ΔT the temperature difference between water inlet and outlet, which is set to 5 K.

2.5. Numerical implementation

The model equations are discretized with the finite volume method. Therefore, the upwind method is used for convective terms and the central differences method for diffusion terms. After the discretization, the model consists of a large differential-algebraic-equation (DAE) system. This DAE-system is implemented and solved using the Julia programming language [48] and the differential equation library Differentialequations.jl [49]. The DImplicitEuler, a 1st order and stiffly stable adaptive implicit Euler solver, is used. Furthermore, the Differentialequations.jl library allows for using callback functions to handle discontinuities, such as the desired down steps in current density.

3. Results and discussion

The simulation results are divided into four sections. First, the cathode hydrogen mass transport coefficient is parameterized with steady-state experimental hydrogen crossover measurements from literature. Further, the influence of the electroosmotic drag on the hydrogen crossover increase is discussed. In section 3.2, the hydrogen crossover dynamics are studied by simulating down steps in current density at different temperatures and pressures. The local 1-D dissolved hydrogen concentration profile in the MEA during steady-state and dynamic operation is considered in more detail in section 3.3. Finally, the influence of the membrane thickness and anode inlet water flow rate on the dynamic hydrogen crossover is examined. All simulations are performed with the Base Case parameter set (supporting information, section S3, Table S1). If a parameter has been changed compared to the Base Case, this is mentioned in the corresponding figure or in the text.

3.1. Model parameterization of the cathode hydrogen mass transport coefficient

In the parameterization step, the cathode hydrogen mass transport coefficient $k_{H_2}^{ccl}$ is assumed constant over the whole current density range and is fitted to steady-state experimental hydrogen permeation measurements from literature. In Fig. 2 the hydrogen permeation measurements from different sources are shown for Nafion 117 [2,11,12], N115 [16] and N212 membrane [12,14,50].

In Fig. 2a, the mass transport coefficient of the model is fitted for low ($k_{H_2}^{ccl} = 3500$ m s^{-1}) and high ($k_{H_2}^{ccl} = 540$ m s^{-1}) experimental hydrogen crossover fluxes with Nafion 117 and 115 membranes. The measurements of Trinke et al. [16] in Fig. 2a were taken at a membrane thickness of 128 μm (N115) and are therefore not directly comparable with a membrane thickness of 178 μm (N117), as they would be lower by a factor of ≈ 0.72. The data of Bernt et al. [12] were measured for different ionomer to carbon ratios (I/C), while others measured for different wt.% of ionomer in the catalyst layer [16]. The higher mass transport coefficient of $k_{H_2}^{ccl} = 3500$ m s^{-1} fits well in the range of the experimental data with low ionomer loadings, (10–20 wt%) [16] and (I/C = 0.6/1) [12]. The steeply increasing hydrogen crossover fluxes [2,11,16] are approximated by a mass transport coefficient of $k_{H_2}^{ccl} = 540$ m s^{-1}.

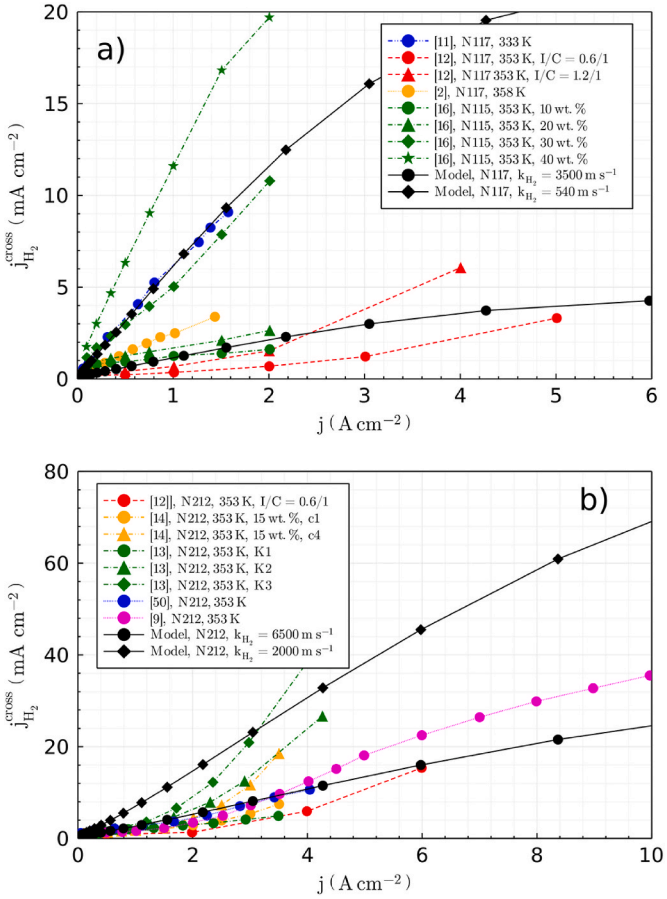

Fig. 2. Experimental measured and simulated hydrogen crossover rates as a function of current density for a) Nafion 115 and 117 and b) Nafion 212 membrane. The simulations were performed at 1 bar and 353 K with constant cathode mass transport coefficients.

In Fig. 2a, the model results show a slight down bending of the hydrogen crossover at high current densities, caused by the influence of the electroosmotic drag [42]. The dragged water carries dissolved hydrogen towards the cathode, acting against the diffusive transport mechanism. Since this convective hydrogen transport depends directly on the applied current density, the hydrogen crossover increase bends down at high current densities (see supporting information, section S5, Fig. S2a). Further, the relative decrease of the hydrogen crossover, caused by the electroosmotic drag, is stronger in thick membranes. The electroosmotic drag does not affect the concentration profile in the cathode catalyst layer, but it does in the membrane (see SI, Fig. S2b), resulting in a nonlinear concentration profile and lower local concentrations in the membrane (see SI, Fig. S2b). These lower local concentrations lead to a lower total hydrogen crossover flux to the anode side.

Fig. 2b depicts experimental hydrogen crossover fluxes for a Nafion 212 membrane [9,12–14,50]. The hydrogen crossover data of Stähler et al. [13] and Martin et al. [14] were measured at different GDL compressions with c1 and K1 referring to the lowest compressions. The measurements of Scheepers et al. [50] and Staehler et al. (K1) [13] are characterized by a linear increase in the hydrogen crossover rate with current density. Therefore, the model with a constant mass transport coefficient of $k_{H_2}^{ccl} = 6500$ m s^{-1} fits in the range of measurements with low compressions and low ionomer contents. However, at high compressions, the measured hydrogen crossover rates display strong nonlinear correlations at current densities above 1 A cm^{-2} [14]. At even higher current densities, the model reproduces the influence of the electroosmotic drag, which was recently measured [9]. The model

results and experimental measurements of Martin et al. [9] are further compared in the supporting information, in section S5, Fig. S3. With the assumption that the data from Staehler et al. (K2, K3) [13] and Martin et al. (c4) [14] would also bend down at higher current densities, the cathode mass transport coefficient was chosen to be $k_{H_2}^{ccl} = 2000$ m s^{-1} to represent quantitatively the upper range of the experimental measurements.

The model with a constant mass transport coefficient cannot reproduce the nonlinear behavior of some experimental measurements. The explanation of the nonlinearities still requires a more sophisticated physics-based model approach with accurate structural information at the nano-/meso-scale, which is not within the scope of this study. Generally, the increase of hydrogen crossover varies quantitatively and qualitatively over a broad range in literature [9,15]. The lower and upper boundaries in H_2 crossover fluxes are captured in the model description by a high and low cathode hydrogen mass transport coefficient.

3.2. Dynamic simulation of current density down steps

In this section, the dynamic behavior of hydrogen permeation is studied. In this regard, the simulations were performed with the Base Case parameters (SI Table S1) and the four different cathode mass transfer coefficients. Different magnitudes of current density down steps are examined. The initial steady-state current densities are determined based on model polarization curves and for an upper operational cell voltage of 2.3 V, providing 4.5 A cm^{-2} for N117 membrane and 11.5 A cm^{-2} for N212 membrane, representing high overload operation (see, SI Figure S4). The current density is reduced at t = 50 s with different magnitudes. The resulting H_2-in-O_2 contents in the anode channel are plotted in Fig. 3 for Nafion® 117 and Nafion® 212, at 353 K and 1 bar as a function of time. The predicted transient peak in H_2-in-O_2 content can be clearly seen. The maximum of the transient hydrogen in oxygen content increases with a larger down step in current density and with a lower mass transport coefficient.

Further, quantitative consideration is given regarding the lower explosion limit (LEL) of 4 vol % hydrogen in oxygen. For Nafion® 117 and a cathode mass transport coefficient of $k_{H_2}^{ccl} = 540\ m\ s^{-1}$, the 50% LEL is reached already at a current density step from 4.5 A cm^{-2} down to 1.62 A cm^{-2}, which represents a shift from a high overload to a close to nominal operation point (1.62 A cm^{-2} at 1.8 V). Going down further in current density, e.g., at 0.35 A cm^{-2}, the transient hydrogen in oxygen content in the anode channel can even reach the lower explosion limit. On the other hand, the transient peaks are not very strong for a high mass transport coefficient (Fig. 3a).

The first thing to notice in Fig. 3b is that all transients with a thinner membrane (N212) are faster. The lower thickness and the higher anode water inlet flow rate for the Nafion® 212, result in a lower residence time in the anode flow channel. As calculated in section 2.4, Nafion® 212 operated at 11.5 A cm^{-2} needs a higher water flow rate to maintain the temperature difference of 5 K between inlet and outlet, due to a higher heat production rate. The influence of the anode inlet water flow rate on the transient is studied in more detail in section 3.4. Furthermore, the transient overshoots are much weaker with Nafion® 212. Only with a low mass transport coefficient ($k_{H_2}^{ccl} = 2000\ m\ s^{-1}$) and a large current density down step, the 50% LEL is transiently exceeded.

Fig. 3c and d compare the hydrogen in oxygen transients in the anode channel and in the anode catalyst layer adjacent to the membrane. The steady-state hydrogen in oxygen contents in the anode catalyst layer are lower than in the channel. Due to the higher diffusion coefficient of hydrogen compared to oxygen, H_2 diffuses faster out of the anode catalyst layer through the PTL into the anode channel than oxygen. The transients in the anode catalyst layer start immediately after the current density step, in comparison to the delayed response in the anode

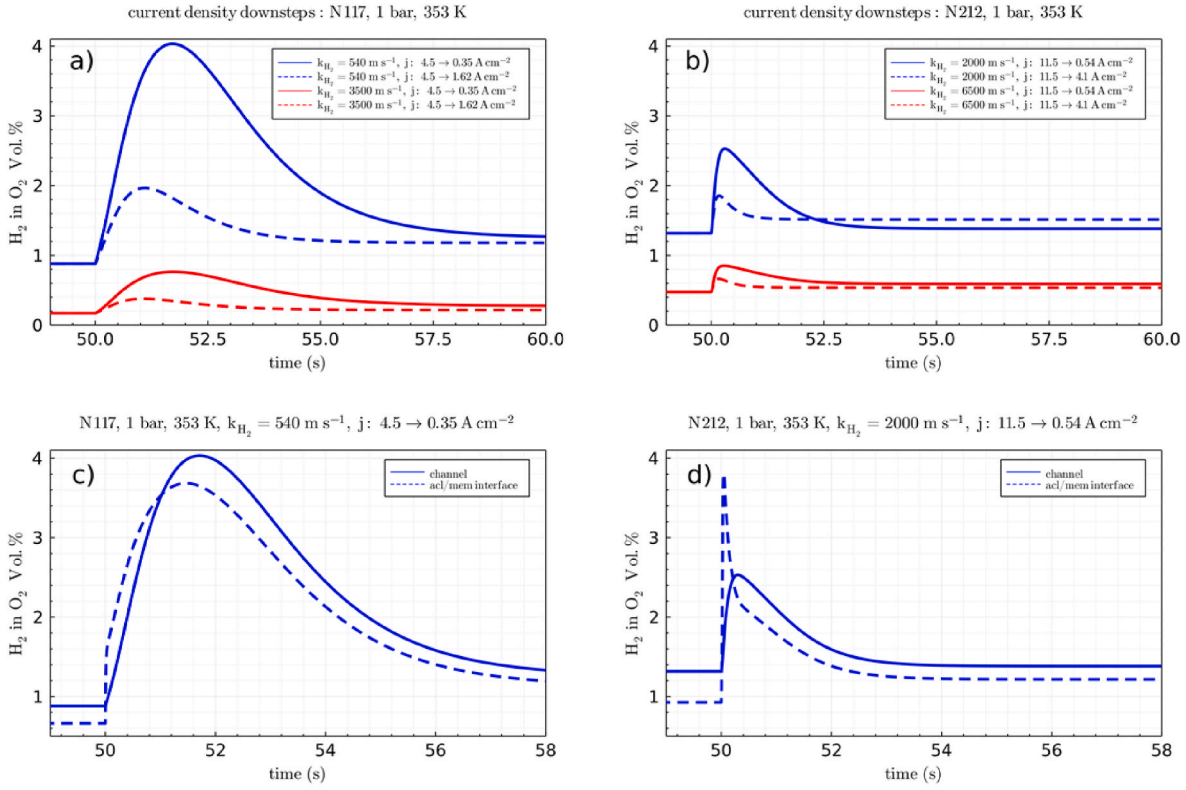

Fig. 3. Dynamic simulation of the hydrogen in oxygen content in the anode channel during current density down steps at 353 K and 1 bar for (a) N117 and (b) N212. The dynamic simulation of the hydrogen in oxygen content during current density down steps in the anode channel are compared to the anode catalyst layer adjacent to the membrane for (c) N117 and (b) N212.

channel. The supersaturated dissolved hydrogen diffuses directly out of the membrane into the anode catalyst layer, which leads to an instantaneous increase at t = 50 s. For the N212 membrane, the instant transient overshoot in the anode catalyst layer is even stronger than in the anode channel, because of the faster discharge of the dissolved H_2 stored in the membrane.

The influence of temperature (Fig. 4a) and pressure (Fig. 4b) on the transient hydrogen overshoots in the anode channel are investigated for the N117 membrane with the lowest cathode mass transport coefficient ($k_{H_2}^{ccl} = 540\ m\ s^{-1}$) and a current density step from an overload of 4.5 A cm^{-2} down to 0.8 A cm^{-2}. The threshold of 0.8 A cm^{-2} represents the lowest possible current density at which the 50% LEL is not exceeded during common steady-state operation conditions (N117, 333 K, 30 bar cathode). The steady-state hydrogen in oxygen content increases with temperature and pressure due to larger dissolved hydrogen diffusion coefficients and the higher cathode hydrogen partial pressures, respectively. Therefore, as temperature rises, transients are accelerated and intensified. Increased cathode pressures enhance hydrogen overshoots, but they do not induce any qualitative change in the transient. A maximum hydrogen in oxygen content of 2.6 vol % is transiently reached in the anode channel (Fig. 4b).

The results of the dynamic simulations suggest that transient overshoots up to several vol. % hydrogen in oxygen can occur, due to down steps in current density, but only for strong cathode mass transport limitations found in cathode catalyst layers with unnecessary high ionomer contents (30–40 wt % [16]) or compression forces [13,14]. The LEL can be transiently exceeded, with large current density down steps, thick membranes, and low cathode mass transport coefficients.

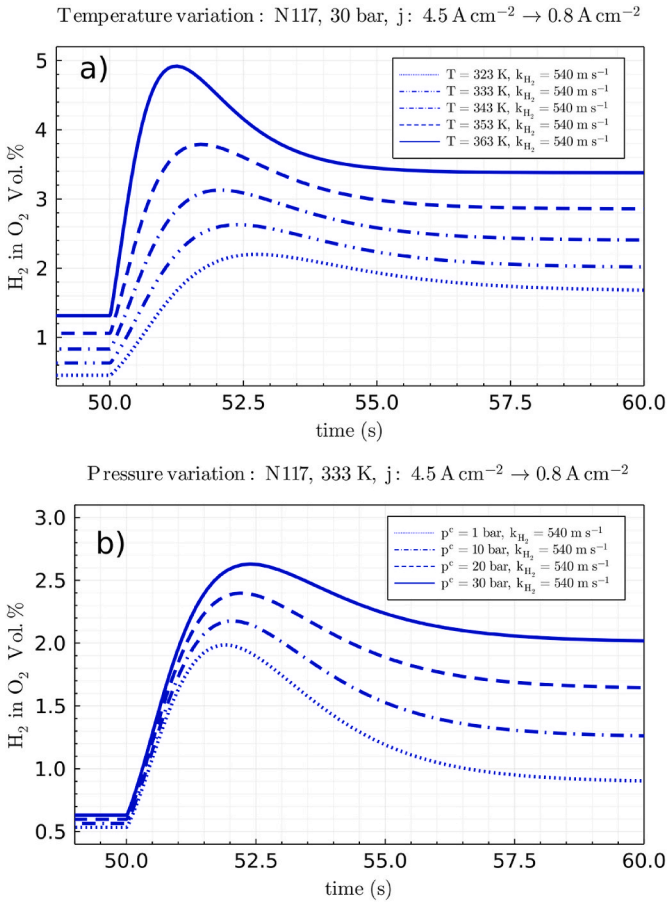

Fig. 4. Influence of temperature (a) and cathode pressure (b) on the transient hydrogen overshoot in the anode channel for an N117 membrane, a cathode mass transport coefficient of $k_{H_2}^{ccl} = 540\ m\ s^{-1}$ during current density step from 4.5 A cm^{-2} down to 0.8 A cm^{-2}.

3.3. Transient through-plane concentration profile

In this section, the 1-D through plane dissolved hydrogen concentration profiles in the catalyst layers and membrane are investigated in more detail. Therefore, a Nafion® 117 membrane is simulated with $k_{H_2}^{ccl} = 540\ m\ s^{-1}$ at 353 K, 1 bar and a current density step from 4.5 A cm^{-2} down to 1.62 A cm^{-2}. The resulting transients in the anode channel and at the anode catalyst layer/membrane interface are shown in Fig. 5a.

The dissolved hydrogen concentration in the through plane view is presented in Fig. 5b, at different times. The x-coordinate is normalized to the thickness of the individual layers for a better visibility of the dissolved hydrogen distribution in the cathode catalyst layer.

The steady-state dissolved hydrogen concentration profiles in the MEA are shown in Fig. 5b at $t_1 = 50$ s (4.5 A cm^{-2}) and $t_5 = 56$ s (1.62 A cm^{-2}). An increase in the dissolved hydrogen concentration in the cathode catalyst layer is clearly visible towards the membrane. This increase is stronger for the steady-state current density of 4.5 A cm^{-2} and starts from a dissolved hydrogen concentration of around 55 mol m^{-3} near the GDL and rises to over 120 mol m^{-3} close to the membrane. This effect can be explained by an increased production rate of hydrogen close to the membrane, due to the proton- and electron conducting

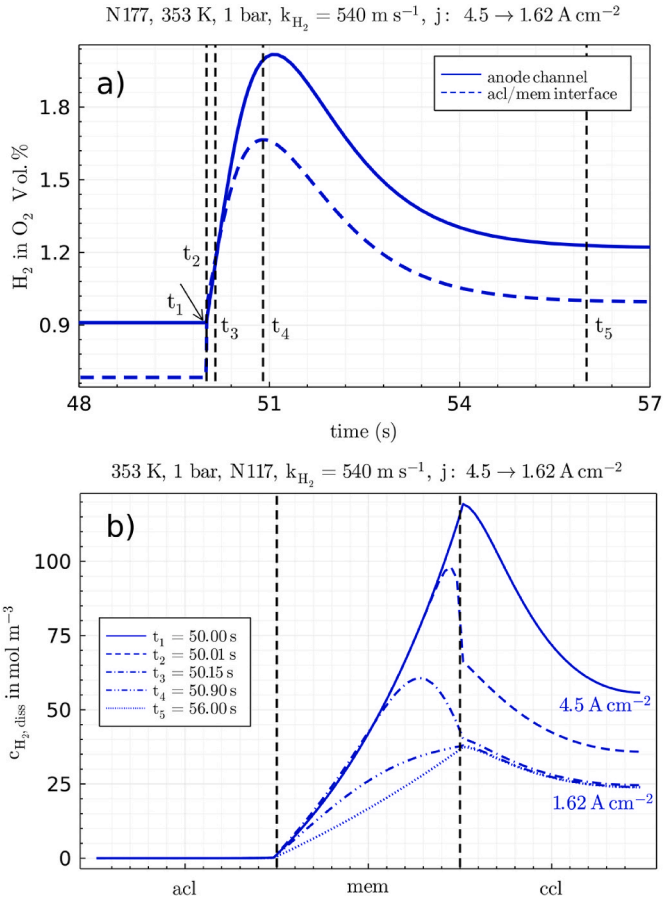

Fig. 5. Dynamic simulation for $k_{H_2}^{ccl} = 540\ m\ s^{-1}$ and a Nafion® 117 membrane with a current density step from 4.5 A cm^{-2} down to 1.62 A cm^{-2}. a) The hydrogen in oxygen content in the anode channel as a function of time with marked time points. b) The 1-D through plane dissolved hydrogen concentration profiles in the catalyst layers and in the membrane at the times marked in (a). The x-coordinates are normalized to the thickness of the individual layers to clearly show the dissolved hydrogen concentration distribution in the cathode catalyst layer.

properties of the catalyst layer [15]. According to the charge balances, the reaction front in the cathode catalyst layer moves closer to the membrane as the proton conductivity of the cathode catalyst layer decreases, in comparison to its electrical conductivity. In the model, the cathode catalyst layer protonic conductivity is one order of magnitude lower than the electrical conductivity (see Table S1 in the SI). This phenomenon can contribute to an upward bending of the hydrogen crossover with current density, but not enough to match strong non-linearities. Furthermore, in both steady-state profiles, the effect of the electroosmotic drag on the dissolved hydrogen concentration can be observed, which deforms an otherwise linear concentration profile in the membrane (Fig. S2 in the supporting information).

At the time $t_2 = 50.01$ s, the dissolved hydrogen dropped almost instantaneously in the cathode catalyst layer, and the dissolved hydrogen in the membrane diffuses out to the anode and cathode sides. As a result, the maximum dissolved hydrogen concentration moves further inside the membrane. At this time, the oxygen production is already lower at the anode, but the membrane is still supersaturated with dissolved hydrogen, resulting in the transient overshot in hydrogen in oxygen content in the anode catalyst layer and channel. At time $t_3 = 50.15$ s, the dissolved hydrogen concentration in the cathode catalyst layer almost reached the new steady state, and the maximum concentration moved even further inside the membrane. The maximum dissolved hydrogen concentration moves closer to the anode and hydrogen diffuses out of the membrane to both sides. At $t_4 = 50.9$ s, the hydrogen in oxygen content in the anode catalyst layer is maximal (Fig. 5a) and most of the dissolved hydrogen has already diffused out of the membrane. With a slight delay, the maximum is also reached in the anode channel. The MEA and the channel attain the new steady after 6 s.

3.4. Influence of membrane thickness and anode inlet water flow rate

The influence of the membrane thickness and the anode water inlet flow rate on the transient hydrogen in oxygen overshot in the anode channel is presented in this section. Both parameters are varied for a current density step of 4.5 A cm^{-2} to 0.35 A cm^{-2} and a mass transport coefficient of $k_{H_2}^{ccl} = 540\ m\ s^{-1}$.

The resulting transients for different membrane thicknesses are depicted in Fig. 6a. The membrane thickness (at 25 °C and RH 50%) is varied from 254 down to 90 μm. The different steady-states in H_2-in-O_2 vol. % in the anode channel are due to the different membrane thicknesses, i.e., the thinner the membrane the higher the steady-state H_2-in-O_2 contents at the same current density. Furthermore, the magnitude of the overshoot increases, and the dynamic response shifts to longer times with membrane thickness, due to the increase of the mass storage capacity. A larger mass storage capacity results in higher dissolved hydrogen amounts that diffuse to the anode side, where the same amount of oxygen is produced regardless of the membrane thickness. On the other hand, the influence of the electroosmotic drag is stronger with thicker membranes (Fig. S2a in the supporting information), lowering the mass storage capacity of dissolved hydrogen, but not enough to skew the influence of membrane thickness. Moreover, the diffusion out of thick membranes requires more time, resulting in longer transients.

The influence of the anode water inlet flow rate is depicted in Fig. 6b. The anode water inlet flow rate is varied from 10.9 ml min^{-1} cm^{-2} in the Base Cases to a minimum and maximum of 0.68- and 43.6-ml min^{-1} cm^{-2}, respectively. The steady-state hydrogen in oxygen content is not influenced by the anode inlet water flow rate. However, the water flow rate has profound effects on the dynamics. At higher inlet water flow rates, stronger and shorter transient hydrogen in oxygen overshoots occur because the residence time in the anode channel decreases, allowing the entire transient to shift to the new steady state more quickly. Meanwhile, the lower gas volume fraction in the anode channel is causing stronger overshoot in the hydrogen in oxygen content, due to the decrease of the dilution effect of the gas phase. In summary, under

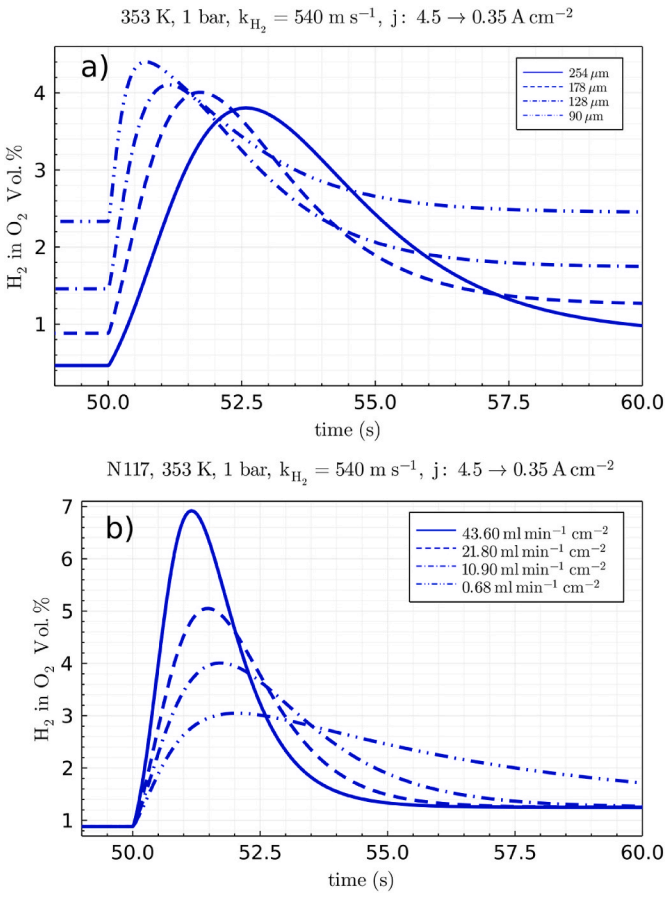

Fig. 6. Dynamic simulation for 1 bar and 353 K with a current density step from 4.5 A cm^{-2} down to 0.35 A cm^{-2} and a cathode mass transport coefficient of $k_{H_2}^{ccl} = 540\ s^{-1}$. a) Transient hydrogen in oxygen concentrations in the anode channel for different nominal membrane thickness. b) Transient hydrogen in oxygen concentrations in the anode channel for different anode water inlet flow rates with Nafion® 117.

the same current density down steps, thicker membranes cause stronger and longer overshoots and higher anode water inlet flow rates stronger but shorter overshoots.

4. Conclusions

A dynamic macroscopic 1-D through-plane model of a PEM electrolysis cell was developed in this work to study for the first time the dynamics of hydrogen crossover. First, the model was parameterized with steady-state hydrogen crossover measurements from literature. The influence of the electroosmotic drag on the dissolved hydrogen concentration decelerates the increase of hydrogen crossover with current density.

Instant down steps in current density were simulated and transient hydrogen in oxygen overshoots on the anode side were clearly seen in all dynamic simulations. The dynamic simulations suggest that an overshoot of up to several vol. % hydrogen in oxygen in the anode can occur, due to down steps in current density, but only for strong cathode mass transport limitations found in cathode catalyst layers with unnecessary high ionomer contents and compression forces.

Under specific conditions with high cathode mass transport limitations, even the 4 vol % lower explosion limit can be transiently reached. For thin membranes, e.g., N212, there is an instantaneous short transient overshoot in the anode catalyst layer, that can be even stronger than in the anode channel. Increase of temperature leads to faster and stronger transient, whereas cathode pressure only enhances the magnitude, but

with higher steady-state hydrogen in oxygen contents after the current density down step. Furthermore, the results indicate that for the same current density down step, thicker membranes and higher anode water inlet flow rates favor stronger hydrogen overshoots due to the larger mass storage capacity for the dissolved gases and lower gas volume fractions in the channel, respectively.

However, strong overshoots reaching the lower explosion limit can be prevented by a careful cathode catalyst design with ionomer contents of around 10–20 wt% and medium MEA compression forces. Nevertheless, it's a matter of discussion whether transiently exceeding the lower explosion limit is a real safety issue, since the small amounts of overshot hydrogen are diluted fast downstream, in the large gas volume of the gas-liquid separator and therefore would not be a thread to safety issues. Apart from the safety perspective, there might be implications regarding catalyst degradation, due to the redox atmosphere during strong overshoots. These may be prevented using recombination interlayers inside the membrane or recombination catalysts in the anode catalyst layer, which are now becoming state of the art.

The presented study highlights the importance of dynamic modeling and simulation as an effective tool to investigate phenomena in advance without building expensive elaborate experimental setups and determine beforehand experimental operating conditions at which the hydrogen overshoot phenomenon can be measured the best.

Nomenclature

a	internal catalyst surface area m^2_{act}/m^3
a_0	catalyst surface area per unit mass of the catalyst m^2_{cat}/g_{cat}
b	Tafel slope V dec^{-1}
c	molar concentration mol m^{-3}
c_p	isobaric specific heat capacity kJ kg^{-1} K^{-1}
D	Diffusion coefficient m^2 s^{-1}
d	thickness m
EW	equivalent weight Kg mol^{-1}
F	Faraday constant C mol^{-1}
$\dot{F}$	volumetric flow rate m^3 s^{-1}
h	height m
j	current density A/m^2_{act}
j_0	local exchange current density A/m^2_{cat}
K	hydraulic permeability m^2
k	mass transport coefficient s^{-1}
k_r	relative permeability
L	loading kg/m^2
l	length m
M	molar mass kg mol^{-1}
$\dot{n}$	molar flux mol m^{-2} s^{-1}
n_{drag}	electroosmotic drag coefficient
p	pressure Pa
p_c	capillary pressure Pa
R	Gas constant J K^{-1} mol^{-1}
S	Solubility coefficient mol m^{-3} Pa^{-1}
s	saturation
T	Temperature K
t	time s
U	voltage V
u	flow velocity m s^{-1}
V	volume m^3
$\overline{V}$	molar volume m^3 mol^{-1}
w	weight fraction
z	through-plane coordinate m

CRediT authorship contribution statement

Tobias Franz: Conceptualization, Methodology, Software, Formal analysis, Investigation, Writing – original draft, Writing – review & editing, Visualization. **Georgios Papakonstantinou:** Conceptualization, Writing – review & editing, Supervision. **Kai Sundmacher:** Conceptualization, Writing – review & editing, Supervision, Funding acquisition.

Declaration of competing interest

The authors declare that they have no known competing financial interests or personal relationships that could have appeared to influence the work reported in this paper.

Data availability

Data will be made available on request.

Acknowledgments

The authors acknowledge the support of this research work by the Research Center of Dynamic Systems (CDS) and the project "Power-to-X Systemmodule", funded by the European Regional Development Fund (ERDF) of the German Federal State Saxony-Anhalt.

Greek letters

α	charge transfer coefficient
Γ	volumetric molar flux mol m^{-3} s^{-1}
γ	surface tension N m^{-1}
$\Delta\varphi^{rev}$	reversible potential V
$\Delta\varphi^{0}$	standard reversible potential V
ε	porosity - η overpotential V
λ	membrane water saturation
μ	dynamic viscosity Pa s
ρ	density kg m^{-3}
σ	conductivity S m^{-1}
τ	turtosity
φ	potential V

Subscripts

a	anode
c	cathode
cat	catalysator
ch	channel
conv	convection
diff	diffusion
diss	dissolved
drag	electroosmotic drag
E	electric
eva	evaporation
g	gas
H_2	hydrogen
H_2O	water
HER	hydrogen evolution reaction
ion	ionomer
l	liquid
mass	mass transport
mem	membrane
O_2	oxygen
OER	oxygen evolution reaction
P	protonic
Pt/C	Platin/Carbon
prod	production
react	reaction
sat	saturated

Superscripts

ach	anode channel
cch	cathode channel
ccl	cathode catalyst layer
eff	effective
in	inlet
out	outlet
sat	saturated

Appendix A. Supplementary data

Supplementary data to this article can be found online at https://doi.org/10.1016/j.jpowsour.2022.232582.

References

[1] P.J. Rheinländer, J. Durst, J. Electrochem. Soc. 168 (2021), 24511, https://doi.org/10.1149/1945-7111/abe0d4.

[2] S.A. Grigoriev, P. Millet, S.V. Korobtsev, V.I. Porembskiy, M. Pepic, C. Etievant, C. Puyenchet, V.N. Fateev, Int. J. Hydrogen Energy 34 (2009) 5986–5991, https://doi.org/10.1016/j.ijhydene.2009.01.047.

[3] M. Schalenbach, M. Carmo, D.L. Fritz, J. Mergel, D. Stolten, Int. J. Hydrogen Energy 38 (2013) 14921–14933, https://doi.org/10.1016/j.ijhydene.2013.09.013.

[4] M. Schalenbach, Int. J. Hydrogen Energy 41 (2016) 729–732, https://doi.org/10.1016/j.ijhydene.2015.11.009.

[5] H. Ito, N. Miyazaki, M. Ishida, A. Nakano, Int. J. Hydrogen Energy 41 (2016) 20439–20446, https://doi.org/10.1016/j.ijhydene.2016.08.119.

[6] B. Bensmann, R. Hanke-Rauschenbach, K. Sundmacher, Int. J. Hydrogen Energy 39 (2014) 49–53, https://doi.org/10.1016/j.ijhydene.2013.10.085.

[7] M. Schalenbach, T. Hoefner, P. Paciok, M. Carmo, W. Lueke, D. Stolten, J. Phys. Chem. C 119 (2015) 25145–25155, https://doi.org/10.1021/acs.jpcc.5b04155.

[8] R. Omrani, B. Shabani, Electrochim. Acta 377 (2021), 138085, https://doi.org/10.1016/j.electacta.2021.138085.

[9] A. Martin, P. Trinke, B. Bensmann, R. Hanke-Rauschenbach, J. Electrochem. Soc. 169 (2022), 94507, https://doi.org/10.1149/1945-7111/ac908c.

[10] P. Trinke, B. Bensmann, R. Hanke-Rauschenbach, Int. J. Hydrogen Energy 42 (2017) 14355–14366, https://doi.org/10.1016/j.ijhydene.2017.03.231.

[11] G. Papakonstantinou, K. Sundmacher, Electrochem. Commun. 108 (2019), 106578, https://doi.org/10.1016/j.elecom.2019.106578.
[12] M. Bernt, J. Schröter, M. Möckl, H.A. Gasteiger, J. Electrochem. Soc. 167 (2020), 124502, https://doi.org/10.1149/1945-7111/abaa68.
[13] M. Stähler, A. Stähler, F. Scheepers, M. Carmo, W. Lehnert, D. Stolten, Int. J. Hydrogen Energy 45 (2020) 4008–4014, https://doi.org/10.1016/j.ijhydene.2019.12.016.
[14] A. Martin, P. Trinke, M. Stähler, A. Stähler, F. Scheepers, B. Bensmann, M. Carmo, W. Lehnert, R. Hanke-Rauschenbach, J. Electrochem. Soc. 169 (2022), 14502, https://doi.org/10.1149/1945-7111/ac4459.
[15] P. Trinke, Experimental and Model-Based Investigations on Gas Crossover in Polymer Electrolyte Membrane Water Electrolyzers, Hannover Institutionelles Repositorium der Leibniz Universität Hannover, 2021.
[16] P. Trinke, G.P. Keeley, M. Carmo, B. Bensmann, R. Hanke-Rauschenbach, J. Electrochem. Soc. 166 (2019) F465–F471, https://doi.org/10.1149/2.0171908jes.
[17] M. Kopp, D. Coleman, C. Stiller, K. Scheffer, J. Aichinger, B. Scheppat, Int. J. Hydrogen Energy 42 (2017) 13311–13320, https://doi.org/10.1016/j.ijhydene.2016.12.145.
[18] A.E. Samani, A. D'Amicis, J.D. de Kooning, D. Bozalakov, P. Silva, L. Vandevelde, IET Renew. Power Gener. 14 (2020) 3070–3078, https://doi.org/10.1049/iet-rpg.2020.0453.
[19] C. Rakousky, U. Reimer, K. Wippermann, M. Carmo, W. Lueke, D. Stolten, J. Power Sources 326 (2016) 120–128, https://doi.org/10.1016/j.jpowsour.2016.06.082.
[20] A. Weiß, A. Siebel, M. Bernt, T.-H. Shen, V. Tileli, H.A. Gasteiger, J. Electrochem. Soc. 166 (2019) F487, https://doi.org/10.1149/2.0421908jes.
[21] G. Papakonstantinou, G. Algara-Siller, D. Teschner, T. Vidaković-Koch, R. Schlögl, K. Sundmacher, Appl. Energy 280 (2020), 115911, https://doi.org/10.1016/j.apenergy.2020.115911.
[22] J.C. Bui, E.W. Lees, L.M. Pant, I.V. Zenyuk, A.T. Bell, A.Z. Weber, Chem. Rev. 122 (2022) 11022–11084, https://doi.org/10.1021/acs.chemrev.1c00901.
[23] B.J. Etzold, U. Krewer, S. Thiele, A. Dreizler, E. Klemm, T. Turek, Chem. Eng. J. 424 (2021), 130501, https://doi.org/10.1016/j.cej.2021.130501.
[24] B. Bensmann, R. Hanke-Rauschenbach, ECS Trans. 75 (2016) 1065–1072, https://doi.org/10.1149/07514.1065ecst.
[25] A.H. Abdol Rahim, A.S. Tijani, S.K. Kamarudin, S. Hanapi, J. Power Sources 309 (2016) 56–65, https://doi.org/10.1016/j.jpowsour.2016.01.012.
[26] B. Han, J. Mo, Z. Kang, G. Yang, W. Barnhill, F.-Y. Zhang, Int. J. Hydrogen Energy 42 (2017) 4478–4489, https://doi.org/10.1016/j.ijhydene.2016.12.103.
[27] A. Zinser, G. Papakonstantinou, K. Sundmacher, Int. J. Hydrogen Energy 44 (2019) 28077–28087, https://doi.org/10.1016/j.ijhydene.2019.09.081.
[28] G. Schmidt, M. Suermann, B. Bensmann, R. Hanke-Rauschenbach, I. Neuweiler, J. Electrochem. Soc. 167 (2020), 114511, https://doi.org/10.1149/1945-7111/aba5d4.
[29] A. Kalinnikov, S.A. Grigoriev, D.G. Bessarabov, K. Bouzek, Electrochim. Acta 387 (2021), 138541, https://doi.org/10.1016/j.electacta.2021.138541.
[30] J.C. Fornaciari, M.R. Gerhardt, J. Zhou, Y.N. Regmi, N. Danilovic, A.T. Bell, A. Z. Weber, J. Electrochem. Soc. 167 (2020), 104508, https://doi.org/10.1149/1945-7111/ab9b09.
[31] P.A. García-Salaberri, J. Power Sources 521 (2022), 230915, https://doi.org/10.1016/j.jpowsour.2021.230915.
[32] T. Vidaković-Koch, T. Miličić, L.A. Živković, H.S. Chan, U. Krewer, M. Petkovska, Curr. Opin. Electrochem. 30 (2021), 100851, https://doi.org/10.1016/j.coelec.2021.100851.
[33] M. Suermann, K. Takanohashi, A. Lamibrac, T.J. Schmidt, F.N. Büchi, J. Electrochem. Soc. 164 (2017) F973–F980, https://doi.org/10.1149/2.13517109jes.
[34] M. Bernt, A. Siebel, H.A. Gasteiger, J. Electrochem. Soc. 165 (2018) F305–F314, https://doi.org/10.1149/2.0641805jes.
[35] A. Stähler, M. Stähler, F. Scheepers, W. Lehnert, M. Carmo, J. Electrochem. Soc. 169 (2022), 34522, https://doi.org/10.1149/1945-7111/ac5c9b.
[36] T. Vidaković-Koch, R. Hanke-Rauschenbach, I. Gonzalez Martínez, K. Sundmacher, C. Breitkopf, K. Swider-Lyons (Eds.), Springer Handbook of Electrochemical Energy, Springer Berlin Heidelberg, Berlin, Heidelberg, 2017, pp. 259–285.
[37] J. Durst, C. Simon, F. Hasché, H.A. Gasteiger, J. Electrochem. Soc. 162 (2014) F190–F203, https://doi.org/10.1149/2.0981501jes.
[38] N. Briguglio, S. Siracusano, G. Bonura, D. Sebastián, A.S. Aricò, Appl. Catal. B Environ. 246 (2019) 254–265, https://doi.org/10.1016/j.apcatb.2018.12.079.
[39] N. Briguglio, F. Pantò, S. Siracusano, A.S. Aricò, Electrochim. Acta 344 (2020), 136153, https://doi.org/10.1016/j.electacta.2020.136153.
[40] C. Klose, P. Trinke, T. Böhm, B. Bensmann, S. Vierrath, R. Hanke-Rauschenbach, S. Thiele, J. Electrochem. Soc. 165 (2018) F1271, https://doi.org/10.1149/2.1241814jes.
[41] S. Garbe, E. Samulesson, T.J. Schmidt, L. Gubler, J. Electrochem. Soc. 168 (2021), 104502, https://doi.org/10.1149/1945-7111/ac2925.
[42] A. Martin, P. Trinke, C. van Pham, M. Bühler, M. Bierling, P.K.R. Holzapfel, B. Bensmann, S. Thiele, R. Hanke-Rauschenbach, J. Electrochem. Soc. 168 (2021), 114513, https://doi.org/10.1149/1945-7111/ac38f6.
[43] Iryna V. Zenyuk, Prodip K. Das, Adam Z. Weber, J. Electrochem. Soc. 163 (2016) F691-F703, https://doi.org/10.1149/2.1161607jes.
[44] I.V. Zenyuk, E. Medici, J. Allen, A.Z. Weber, Int. J. Hydrogen Energy 40 (2015) 16831–16845, https://doi.org/10.1016/j.ijhydene.2015.08.009.
[45] H. Kraus, Die Atmosphäre der Erde: Eine Einführung in die Meteorologie, 3. erw. und aktualisierte Aufl, Springer, Berlin, 2004.
[46] T.A. Zawodzinski, J. Davey, J. Valerio, S. Gottesfeld, Electrochim. Acta 40 (1995) 297–302, https://doi.org/10.1016/0013-4686(94)00277-8.
[47] H. Kim, M. Park, K.S. Lee, Int. J. Hydrogen Energy 38 (2013) 2596–2609, https://doi.org/10.1016/j.ijhydene.2012.12.006.
[48] J. Bezanson, A. Edelman, S. Karpinski, V.B. Shah, SIAM Rev. 59 (2017) 65–98, https://doi.org/10.1137/141000671.
[49] C. Rackauckas, Q. Nie, JORS 5 (2017) 15, https://doi.org/10.5334/jors.151.
[50] F. Scheepers, M. Stähler, A. Stähler, E. Rauls, M. Müller, M. Carmo, W. Lehnert, Improving the Efficiency of PEM Electrolyzers through Membrane-specific Pressure Optimization, 2020.